Research Article Vol. 27, No. 14 | 8 Jul 2019 | OPTICS EXPRESS 19309

Optics EXPRESS

High-rate photon pairs and sequential Time-Bin entanglement with Si_3N_4 microring resonators

FARID SAMARA,[1,3] ANTHONY MARTIN,[1] CLAIRE AUTEBERT,[1] MAXIM KARPOV,[2] TOBIAS J. KIPPENBERG,[2] HUGO ZBINDEN,[1] AND ROB THEW[1,*]

[1] *Group of Applied Physics, University of Geneva, Geneva, Switzerland*
[2] *Swiss Federal Institute of Technology Lausanne, CH-1015, Switzerland*
[3] *farid.samara@unige.ch*
[*] *robert.thew@unige.ch*

Abstract: Integrated photonics is increasing in importance for compact, robust, and scalable enabling quantum technologies. This is particularly interesting for developing quantum communication networks, where resources need to be deployed in the field. We exploit photonic chip-based Si_3N_4 microring resonators to realise a photon pair source with low-loss, high-noise suppression and coincidence rates of 80×10^3 s^{-1}. A simple photonic noise characterisation technique is presented that distinguishes linear and nonlinear contributions useful for system design and optimisation. We then demonstrate an all-fiber 750 MHz clock-rate sequential Time-Bin entanglement scheme with raw interference visibilities > 98 %.

1. Introduction

Integrated photonics allows one to realise optical devices that are robust, compact and scalable, thus motivating the increasing interest in research and development of integrated optical components for both the classical and quantum communication domains [1, 2]. In particular, integrated sources of single and entangled photons at telecommunication wavelengths [3, 4] are an essential resource for the field of quantum communication [5].

By exploiting the nonlinear processes of spontaneous parametric down-conversion (SPDC) or spontaneous four-wave mixing (SFWM), such photon sources have been demonstrated in a variety of integrated photonic structures, including periodically poled nonlinear crystals [2], strip waveguides [6, 7], disks [8, 9] and ring resonators [10, 11]. Among the different approaches, a particularly promising one is the use of SFWM in microring resonator (MRR) cavities. Indeed, a significant practical advantage is provided due to the field enhancement offered by the MRR cavity, which reduces the required pump power to the milliwatt or even the microwatt regime [12].

MRR devices generate correlated photon pairs distributed over a frequency-comb, corresponding to the cavity resonances around the pump wavelength. This frequency comb structure can be matched to different DWDM channels to multiplex the entanglement [10, 13] or to generate high-dimensional frequency entangled quantum states [14–16] which can be used for quantum computation [17, 18]. Additionally, optical cavities, such as MRR, can produce inherently narrow bandwidth photons [19, 20] without the need for narrowband filters, which can introduce unwanted loss. SFWM in MRR structures have demonstrated photon bandwidths down to 30 MHz [21]. Such narrow photon bandwidths are well adapted to the acceptance bandwidth of quantum memories [22], thus they are important in the application of quantum networks.

Silicon photonics is a commonly employed platform for integrated photon pair sources due to its high third-order non-linearity and CMOS-compatibility, with numerous silicon-MRR photon pair sources demonstrated so far [12, 23–27]. While making great progress in recent years, and generally achieving excellent results, silicon-MRR can be limited by two-photon absorption at telecom wavelength due to a relatively low bandgap [11]. This effect is even more pronounced in

#363175 https://doi.org/10.1364/OE.27.019309
Journal © 2019 Received 25 Mar 2019; revised 22 May 2019; accepted 23 May 2019; published 25 Jun 2019

MRR due to the field enhancement associated with the cavity, resulting in a limitation on the effective Q-factor. In contrast, silicon nitride (Si_3N_4) and high-index doped silica (Hydex) [28] provide promising alternative platforms due to their CMOS-compatibility and absence of two-photon absorption in the telecommunication band, with several recent demonstrations of MRR based photon pair sources for both platforms [14,21,29–32]. In particular, we focus on the Si_3N_4 platform, which due to recent advances in the fabrication of ultra-low-loss waveguides [33,34], flexible dispersion engineering [35] and fiber-to-chip coupling techniques [36], has become one of the key platforms for nonlinear integrated photonics. A prominent example of its application are photonic-chip-based soliton microcombs [37,38], which have enabled the generation of broadband coherent optical combs with high repetition rates in fully integrated devices amenable for wafer-scale manufacturing.

In this paper, we study integrated photon-pair sources based on Damascene process MRR as well as introducing a novel approach for studying unwanted photonic noise in SFWM sources in general. High photon pair detection rates were achieved thanks to efficient noise filtering. Additionally, we exploit a Si_3N_4 MRR to demonstrate a high repetition rate sequential Time-Bin scheme [39] well suited for quantum communication applications.

2. Experimental set-up

Figure 1 illustrates the set-up used for the photon pair generation and detection, in addition to the set-up for sequential Time-Bin entanglement analysis. The MRR under test has a Q-factor of 4.6×10^5, which gives a good trade-off between brightness and stability: higher Q-factors lead to brighter sources but narrower resonance linewidths, and hence, are more challenging to maintain on-resonance without sophisticated stabilisation schemes [29,40]. This also results in relatively short coherence times allowing for high repetition rates, e.g. for the sequential Time-Bin entanglement scheme. For the moderate Q-factor devices used here, thermal stabilisation of the chip was enough to ensure on-resonance operation. The free spectral range (FSR) of the device is 192.37 GHz, which is sufficiently close to the standard 200 GHz DWDM channel spacing for low-loss filtering. The resonances structure can be thermally tuned (-2.75 GHz/K) to achieve the correct matching with the DWDM channels.

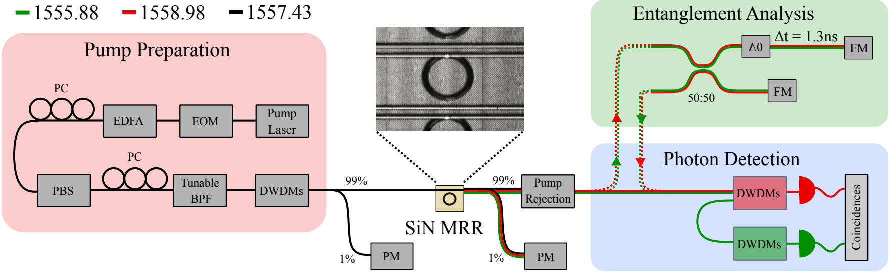

Fig. 1. Experimental schematic. On the left is the pump laser preparation which is then injected into the Si_3N_4 MRR. On the right, we have the set-up for characterising the source and a folded Michelson interferometer for analysing the sequential Time-Bin entanglement. EOM: electro-optical modulator; EDFA: erbium doped fiber amplifier. PC: polarisation controller. PBS: fiber polarising beam-splitter. BPF: Band-Pass Filter. PM: power meter. FM: Faraday mirror.

In the first instance, we use a continuous-wave (CW) pump laser (DL100 Toptica) at a wavelength of $\lambda = 1557.43$ nm corresponding to the middle of the ITU channel 25. The pump can be modulated by an electro-optical modulator (EOM), thus giving rise to pulses which are used to generate sequential Time-Bin entanglement [41]. The pulse width and the repetition rate can be fixed by choosing the corresponding radio frequency (RF) signal that drives the EOM. Subsequently, we use an erbium-doped fiber amplifier (EDFA) to achieve the desired amount of power. A set of polarisation controllers and a polarising beam splitter (PBS) are used to control the polarisation coupled into the waveguide. To remove the amplified spontaneous emission of the pump (laser + EDFA), a pump filtering stage is employed, consisting of a tunable bandpass filter (25 GHz at FWHM) and two 100 GHz DWDM filters which give a pump isolation of 135 dB.

Light is coupled in and out of the chip using inversely tapered (1-D) bus waveguides and anti-reflection (AR) coated lensed fibers with a spot-size diameter of 5 μm. The chip to lensed-fiber coupling losses at both facets are continuously monitored by collecting 1 % of the light at the input and the output of the chip; on average, the input to output losses are 6 dB. If we neglect the propagation loss inside the bus waveguide, and assume equal coupling losses for the input and output facets, then we get 3 dB of coupling loss per facet. At the output of the chip, a set of DWDMs is employed to reject the pump and select the photons of interest.

The detection scheme is based on free-running superconducting nanowire single-photon detectors (SNSPDs) [42] with a detection efficiency of 80 % and dark count rate of 40 s^{-1} whose signals are sent to a time-to-digital-converter (IDQ-ID800) to record the coincidences histogram.

3. Photon pair source characterisation

In the following we characterise the source, in particular, we present a novel approach to determine various photonic sources of noise in the system, as well as pair generation rates and the purity of the emitted photons.

3.1. *Photonic noise on and off the chip*

Ideally, the source should generate only correlated photon pairs, however, in such an experiment there are several sources of unwanted photonic noise that can degrade their quality or the subsequent entanglement measurement. In our experiment, we can identify two main categories of photonic noise: the first is related to the set-up without the Si_3N_4 MRR chip, while the second is due to the MRR chip itself, and in particular, only when the pump wavelength is tuned on-resonance. In the following, we refer to all types of uncorrelated photons as "photonic noise" and we first try to understand their origins, and subsequently, to minimise their contribution.

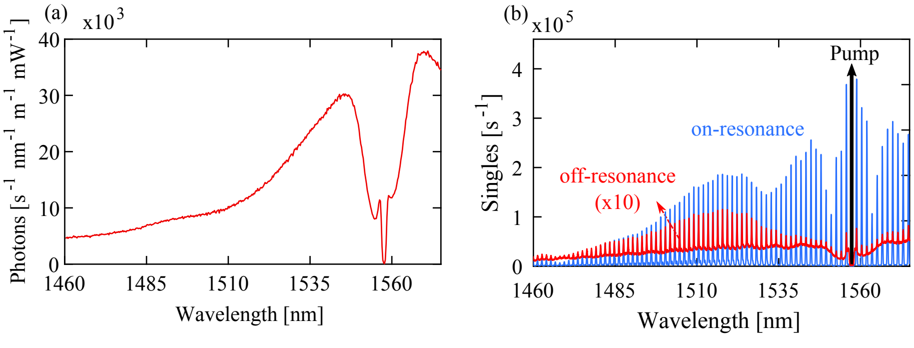

Fig. 2. (a) Spontaneous Raman scattering generated by the set-up without the MRR. It is possible to observe two dips around the pump wavelength of 1557.43 nm; A narrow dip due to the pump rejection filters, and a wide dip due to spontaneous Raman scattering in the fibers. (b) The spectral response of the MRR for both on- and off-resonance cases.

In the first case, we investigate the noise introduced by the experimental set-up by bypassing the MRR device. To characterise the spectrum of the photonic noise we consider either the signal or idler path, and replace the DWDM filters of the photon detection stage (see Fig. 1) with a tunable bandpass filter with a bandwidth of 25 GHz combined with a set of 200 GHz notch filters (not shown in Fig. 1). The combination of these filters provides a total pump rejection of 110 dB. The noise spectrum is presented in Fig. 2(a). We observe that the pump laser (around 1557 nm) residue is negligible, however, elsewhere, there is a broad spectral envelope resembling that of typical Raman scattering in fiber [43]. By varying the pump power and fiber length we determine a linear scaling, in keeping with the hypothesis of Raman generated noise. To mitigate this noise, we shortened the fibers between the pump cleaning and pump rejection filters down to a minimum practical length of around 50 cm in total.

Having studied the photonic noise related to the fiber elements of our set-up, we now turn our attention to studying the extra contribution that is introduced by the MRR Si_3N_4 chip. For this, we insert the MRR chip back in the set-up and observe the single photon counts when the pump wavelength is tuned both *off* and *on* the cavity resonance wavelength, as shown in Fig. 2(b). We can clearly see the comb structure associated with the MRR emission, which spans around 60 frequency comb lines on the blue-shifted side of the pump. A similar spectrum exists on the red-shifted side, however, this is outside the range of our tunable filter.

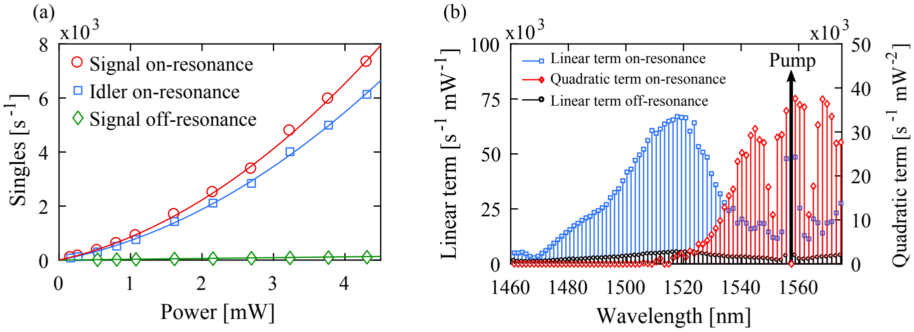

Fig. 3. (a) Detected photons (Singles) as a function of injected laser pump power for both the *off* and *on* resonance cases. For the off-resonance case, only the singles from the signal wavelength are shown. (b) The singles as a function of power for each resonant line is separated into its linear and quadratic terms.

To distinguish the contributions of photonic noise and the correlated photon pairs of interest, i.e. SFWM, we measure the spectral response for different pump powers at the input of the MRR. Figure 3(a) shows the number of detections as a function of pump laser power for the two frequency channels neighbouring the pump, i.e. the target signal and idler wavelengths. We can then fit this data with a function of the form: $a\,P + b\,P^2$, where P correspond to the injected pump power. The photonic noise due to the linear process can be associated with the coefficient a, and the quadratic contribution of photons generated by SFWM with b. Overall, the off-resonance linear noise contribution is comparable to the case with no chip, around $a = 2.5 \times 10^3\ \mathrm{s^{-1}\ mW^{-1}}$, however, on-resonance the noise significantly increases to $a = 59 \times 10^3\ \mathrm{s^{-1}\ mW^{-1}}$. In comparison, we find $b = 26 \times 10^3\ \mathrm{s^{-1}\ mW^{-2}}$ for the quadratic contribution in the signal channel. The on-resonance linear contribution indicates that there is extra photonic noise generated by the MRR chip.

In Fig. 3(b), we extend this analysis to the individual frequency channels, repeatedly measuring each channel for varying pump powers and extracting the linear and quadratic contributions. For the on-resonance case, we see that while the SFWM term is high for the resonant lines adjacent to the pump wavelength, there is also significant linear noise due to broadening of the pump introduced by second-order non-linear effects. For the off-resonant case, only the linear term is reported in Fig. 3(b) since the quadratic term is negligible.

The spectral shape of the linear noise contribution resembles that reported for fiber [43], however, it is not obvious that this can be completely attributed to a Raman process. One also needs to consider the role of the SiO_2 substrate and tighter confinement of the MRR. Recently, Raman-like spectra have been, at least partially, attributed to thermo-refractive noise in amorphous materials such as Si_3N_4 waveguides [44]. A better understanding of the origins could further assist in optimising the fabrication of these devices and their exploitation as low-noise photon pair sources. Nonetheless, this way to analyse the photonic noise provides a practical approach to identify the best DWDM channels to maximise the signal to noise ratio and CAR.

3.2. Photon pair generation

To characterise the photon pair generation we use the analysis setup illustrated in the lower right corner of Fig. 1. Now that there is no need to tune filters as for the noise analysis, the signal, and idler photons are collected with two band-pass (200 GHz) DWDMs in the frequency channels immediately around the pump at 1558.98 nm (ITU23) and 1555.88 nm (ITU27), respectively, with an additional notch DWDM filter and a fiber Bragg grating, which achieves a pump rejection of 145 dB with a signal and idler isolation of 100 dB.

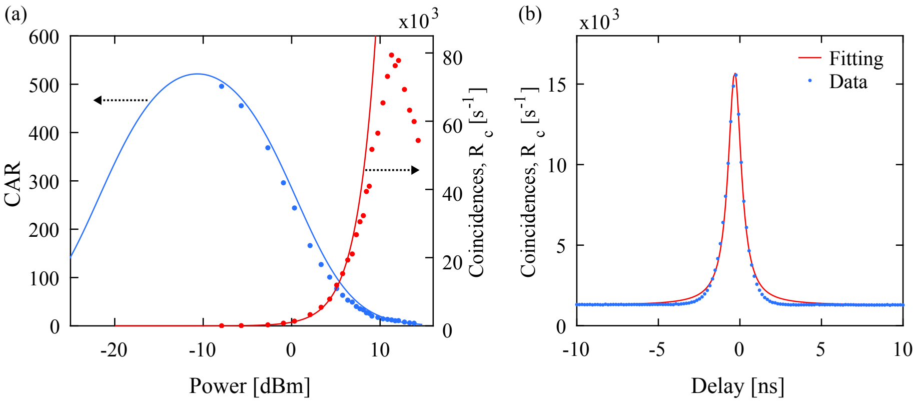

Fig. 4. (a) Coincidence count rate R_c and coincidence-to-accidental ratio CAR as a function of the pump laser power. The predicted CAR and the quadratic fitting of the coincidences at low power (before detector saturation) are given by solid lines. (b) The coincidence histogram corrisponding to maximum photon pair detection rate of 80×10^3 s^{-1}.

The presence of correlated photon pairs was demonstrated by acquiring the coincidence histogram between the signal and idler detections and observing the coincidence peak at zero delay. The coincidence count rates, R_C, and the coincidences-to-accidental ratio, CAR, as a function of the injected pump power are shown in Fig. 4(a). The values for R_C and CAR that are reported in this paper are extracted from the corresponding coincidences histogram by considering a FWHM (320 ps) time window. We see that for pump powers below 5 mW, the coincidence count rate scales with the square of the pump power, thus confirming that the generated pairs are coming from the SFWM process. However, as the pump power is further increased, we enter the count rate saturation region of the SNSPDs where the effective detection efficiency begins to drop as the detectors do not have time to recover their full efficiency. The recovery time of our detectors is on the order of 100 ns, limited by the electronic circuitry of the SNSPDs. The detectors saturation explains the deviation of the coincidence count rate from the quadratic scaling for pump powers above 5 mW. This is exacerbated due to the relatively high linear photonic noise that produces singles but no coincidence counts. Nonetheless, with a pump power of 13.5 mW, we obtain a maximum photon pair detection rate of 80×10^3 s^{-1} with a corresponding CAR of 12.3 (see Fig. 4(b)).

To understand the limiting factors on the CAR, also shown in Fig. 4(a), we calculated the expected behaviour of the CAR as a function of the laser pump power (see [45] for example) based on the photonic noise found in Sec. 3.1. The CAR prediction agrees with the experimental data. It shows a reduction of CAR at high pump power due to double pair generation. At low pump power, the CAR is mainly limited by the detector's dark counts. The highest CAR value of 495 was obtained by injecting 160 μW of pump power, however, this corresponds to a relatively low coincidence detection rate of 29.5 s^{-1}. It is worth mentioning that these numbers indicate a range of operation, which in any case would need to be optimised for a given experiment.

We can relate the pair generation rate (PGR) to the singles for the signal S_s, idler S_i and coincidences R_c by $PGR = S_i S_s / R_c$ [46]. By considering only the singles due to SFWM, i.e. the quadratic terms from the fittings in Fig. 3(a) and the R_c from the fitting of Fig. 4(a), we estimate a PGR of $5.2 \times 10^5\ s^{-1}\ mW^{-2}$. The photons bandwidth and coherence time can be derived from the coincidence histogram, or the resonance line-width, which gives 445 MHz and 320 ps respectively, giving a source brightness of $1.2 \times 10^3\ s^{-1}\ MHz^{-1}\ mW^{-2}$. One should note that the brightness should only be compared to $\chi^{(3)}$ sources as the definition is different for $\chi^{(2)}$ sources. Similarly, MRR sources are highly dependant on the Q-factor of the resonator, which should be optimised for the target application. For example, here we chose a Q-factor on the order of 10^5 so we can exploit a high Time-Bin entanglement repetition rate. In comparison, Ramelow *et. al.* [21] obtained a PGR of $3.9 \times 10^6\ s^{-1}\ mW^{-2}$ for 90 MHz photons from a MRR device with a $Q = 2 \times 10^6$. Finally, the total loss in each of the signal and idler paths can be estimated from the ratio between the measured singles and coincidence counts [46], which give 13.05 dB and 13.84 dB for signal and idler respectively. This total loss includes the propagation losses inside the MRR, the coupling loss, filter losses, and the finite efficiency of the detectors.

3.3. Photon purity

Pure, or spectrally uncorrelated, photon-pairs are essential for the realisation of efficient multi-photon experiments such as teleportation or entanglement swapping. By generating pure photons, there is no need to use extra, and typically lossy, spectral filtering to ensure that photons from different sources are indistinguishable - having a high HOM dip visibility [47]. n.b. the filter bandwidths used here are much larger than that of the photons such that the photons are distributed into their respective wavelength (DWDM) channels, but not spectrally filtered. The state's spectral purity can be determined by measuring the second-order auto-correlation function - $g^{(2)}(0)$ - in a Hanbury Brown and Twiss like experiment [48] by sending the signal (or idler) photons onto a 50:50 beam-splitter and measuring the coincidence detections between the outputs [49].

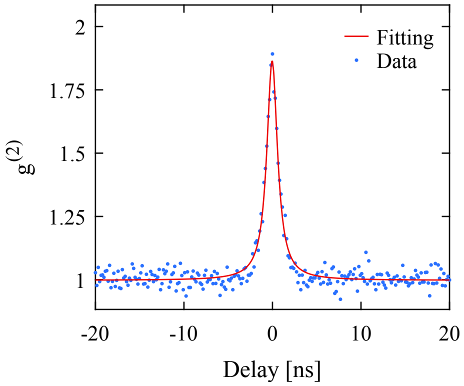

Fig. 5. The auto-correlation coincidence histogram, from which we can extract the purity of the generated photons.

For a pure state, we expect a $g^{(2)}(0)$ close to 2, which corresponds to thermal statistics typical of a single mode. When the number of modes increases $g^{(2)}(0)$ tends to 1, which is the signature of a Poissonian distribution. The results of the $g^{(2)}(0)$ measurement is reported in Fig. 5. The data was fitted with a Lorentzian function, from which we calculated $g^{(2)}(0)$ of 1.86 ± 0.07 (taken as the ratio between the coincidences at zero-delay and the background). The photon purity can also be quantified by the Schmidt number n [45, 49], which is related to the auto-correlation function by $g^{(2)}(0) = 1 + 1/n$. From a $g^{(2)}(0)$ of 1.86 ± 0.07 we find $n = 1.16 \pm 0.11$.

4. Sequential Time-Bin entanglement

The advantage of Time-Bin entanglement, compared to Energy-Time, is the ability to synchronise independent sources for more complex communication tasks while keeping the advantage of phase encoding. We start by using an electro-optical modulator (EOM), as shown in Fig. 1, to pulse the pump laser such that photon pairs are created in superpositions of different times. The CW laser ensures that coherence is maintained over these time-bins such that we generate states of the form,

$$|\psi\rangle \propto |t_i, t_i\rangle_{\omega_1\omega_2} + e^{i\phi}|t_{i+1}, t_{i+1}\rangle_{\omega_1\omega_2}. \tag{1}$$

Rather than sending each laser pulse through a “Time-Bin interferometer”, we use each sequential pair of laser pulses to define the time bins, such that the laser pulse rate can be fully exploited. To characterise the entanglement we need to pass the pairs through imbalanced interferometers with a path-length difference Δt corresponding to the laser’s periodicity. In this experiment we use a device with a slightly lower Q-factor of 1.1×10^5 to ensure that the coherence time of the generated photons $\tau_c \approx 86\,\text{ps} \ll \Delta t$. This then allows us to operate with a clock rate for the pulsed laser of 750 MHz, i.e. with $\Delta t = 1.33\ ns$.

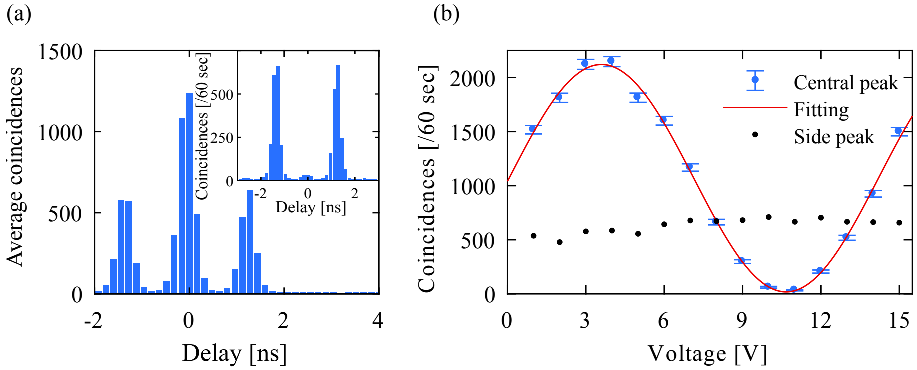

Fig. 6. (a) The phase averaged coincidence histogram, and the coincidence histogram corresponding to maximum destructive interference (insert). (b) Coincidence counts in the central and side histogram peaks as a function of the phase - voltage on the piezo.

Typically, in such an experiment, each photon of a pair is sent to an individual interferometer, however, for simply certifying the entanglement it is sufficient to send both photons of the pair into an imbalanced Michelson fiber interferometer, as shown in the top right of Fig. 1. The interferometer is temperature stabilised and a piezo is used to vary the relative phase between the two arms ($\Delta\phi$).

In Fig. 6(a), we can see the characteristic three temporal peaks clearly defined in the coincidence histogram, where we post-select only the central one, which corresponds to a measurement of the state of Eq. (1). The coincidence counts in the central peak are integrated for 60 s for each phase setting giving rise to the interference curve in Fig. 6(b). From the fitting, we extracted a raw visibility of $98.29 \pm 0.20\,\%$ and a net visibility of $99.96 \pm 0.03\,\%$. The inset in Fig. 6(a) shows the the coincidence histogram at maximum destructive interference, i.e. at 11 V in Fig. 6(b). In contrast, no interference is observed in the coincidence counts of the side peaks. These results clearly demonstrate a high degree of entanglement. We see that the system achieves a coincidence rate of around $R_c \sim 16\,\mathrm{s}^{-1}$ for 10 mW of injected pump power. It is worth mentioning that the coincidence rate reported here is 3 order of magnitude lower than the one reported in Sec. 3.2 for the same pump power. This is due to the fact that here we chose a lower Q-factor device (PGR and $R_c \propto Q^3$) in order to realize the 750 MHz repetition rate for Time-Bin entanglement generation. Additionally, the interferometer introduces 9 dB of extra loss, with 6 dB due to the fact that we collect the pair on one arm of the beam splitter. Selecting only the coincidences in the central peak of the histogram (Fig. 6(a)) introduces 3 dB of extra loss.

5. Discussion

We have demonstrated a Si_3N_4 MRR scheme for generating photon pairs and sequential Time-Bin entanglement that has relatively low losses, with excellent pump extinction and pair isolation. The noise analysis developed here provides a useful tool to identify frequency channel pairs that have the best CAR. While spurious photonic noise from the associated set-up, principally in the fibers, was largely suppressed, photonic noise from the Si_3N_4 MRR remains and warrants further investigation to better understand its origins and potential mitigation solutions. Nonetheless, the resulting sequential Time-Bin entanglement (raw) visibility >98 % and pair coincidence rates of $80 \times 10^3\,\mathrm{s}^{-1}$ indicate this is not a fundamentally limiting factor for the visibilities and coincidences rate, since some of this noise is naturally removed through coincidences. However, both could be improved by lowering the noise generated in the fibers and by the MRR device.

It is important to differentiate the performance of the MRR device and that of the overall source. The fiber generated noise is only critical between the pump cleaning and pump rejection filters, and hence needs to be as short as possible. On the other hand, the rest of the fiber has no effect on the overall performance of the source and this all-fiber configuration demonstrates the potential of this approach for compact, even rack-mounted, systems, by allowing the easy connectivity of simple, lasers, amplifiers and filtering systems. The performance of these devices is increasingly comparable with more mature technologies, such as PPLN [2], with the benefit of using a telecom wavelength pump that is advantageous for distributed quantum communication scenarios.

The recent progress on high-Q MRR in Si_3N_4 [34] could also provide an avenue for more complex quantum communication tasks such as multiphoton entanglement swapping experiments, or coupling to quantum memories. An area where significant impact could be made is in better mode matching between the fiber and bus waveguide for fiber pigtailing, which would be important to increase both the coupling and heralding efficiencies. The device and system performance could also be further improved as well by optimising the coupling between the bus waveguide and MRR cavity [50], or with more complex structures [51], which would also allow us to exploit the high Q-factor cavities and 2-D tapers [52] that are achievable using the damascence process in Si_3N_4.

We have demonstrated a compact all-fiber scheme for photon pair generation, with robust operation, only requiring passive temperature stabilization. These results, along with recent demonstrations of quantum frequency conversion [53] and CMOS compatible fabrication represent a promising and scalable path forward for Si_3N_4 as a key enabling quantum technology.

Funding

Swiss National Science Foundation (SNF) (182664, 161573); Defense Advanced Research Projects Agency (DARPA) (HR0011-15-C-0055); European Space Agency (ESA) (4000116145/16 /NL/MH/GM).

Acknowledgments

The authors would like to thank M. Perrenoud, M. Caloz and F. Bussières for development of the SNSPDs.

References

1. A. Politi, J. C. F. Matthews, M. G. Thompson, and J. L. O'Brien, "Integrated quantum photonics," IEEE J. Sel. Top. Quantum Electron. **15**, 1673–1684 (2009).
2. S. Tanzilli, A. Martin, F. Kaiser, M. P. De Micheli, O. Alibart, and D. B. Ostrowsky, "On the genesis and evolution of integrated quantum optics," Laser Photonics Rev. **6**, 115–143 (2011).
3. J. L. O'brien, A. Furusawa, and J. Vučković, "Photonic quantum technologies," Nat. Photonics **3**, 687–695 (2009).
4. M. D. Eisaman, J. Fan, A. Migdall, and S. V. Polyakov, "Invited review article: Single-photon sources and detectors," Rev. Sci. Instrum. **82**, 071101 (2011).
5. N. Gisin and R. Thew, "Quantum communication," Nat. Photonics **1**, 165–171 (2007).
6. H. Takesue, Y. Tokura, H. Fukuda, T. Tsuchizawa, T. Watanabe, K. Yamada, and S. I. Itabashi, "Entanglement generation using silicon wire waveguide," Appl. Phys. Lett. **91**, 201108 (2007).
7. X. Zhang, Y. Zhang, C. Xiong, and B. J. Eggleton, "Correlated photon pair generation in low-loss double-stripe silicon nitride waveguides," J. Opt. **18**, 074016 (2016).
8. M. Förtsch, J. U. Fürst, C. Wittmann, D. Strekalov, A. Aiello, M. V. Chekhova, C. Silberhorn, G. Leuchs, and C. Marquardt, "A versatile source of single photons for quantum information processing," Nat. Commun. **4**, 1818 (2013).
9. X. Lu, S. Rogers, T. Gerrits, W. C. Jiang, S. W. Nam, and Q. Lin, "Heralding single photons from a high-Q silicon microdisk," Optica **3**, 1331–1338 (2016).
10. F. Mazeas, M. Traetta, M. Bentivegna, F. Kaiser, D. Aktas, W. Zhang, C. A. Ramos, L. A. Ngah, T. Lunghi, É. Picholle, N. Belabas-Plougonven, X. Le Roux, É. Cassan, D. Marris-Morini, L. Vivien, G. Sauder, L. Labonté, and S. Tanzilli, "High-quality photonic entanglement for wavelength-multiplexed quantum communication based on a silicon chip," Opt. Express **24**, 28731–28738 (2016).
11. A. Pasquazi, M. Peccianti, L. Razzari, D. J. Moss, S. Coen, M. Erkintalo, Y. K. Chembo, T. Hansson, S. Wabnitz, P. Del'Haye, X. Xue, A. M. Weiner, and R. Morandotti, "Micro-combs: A novel generation of optical sources," Phys. Rep. **729**, 1–81 (2018).
12. M. Savanier, R. Kumar, and S. Mookherjea, "Photon pair generation from compact silicon microring resonators using microwatt-level pump powers," Opt. Express **24**, 3313–3328 (2016).
13. M. Fujiwara, R. Wakabayashi, M. Sasaki, and M. Takeoka, "Wavelength division multiplexed and double-port pumped time-bin entangled photon pair generation using si ring resonator," Opt. Express **25**, 3445–3453 (2017).
14. P. Imany, J. A. Jaramillo-Villegas, O. D. Odele, K. Han, D. E. Leaird, J. M. Lukens, P. Lougovski, M. Qi, and A. M. Weiner, "50-GHz-spaced comb of high-dimensional frequency-bin entangled photons from an on-chip silicon nitride microresonator," Opt. Express **26**, 1825–1840 (2018).
15. M. Kues, C. Reimer, P. Roztocki, L. R. Cortés, S. Sciara, B. Wetzel, Y. Zhang, A. Cino, S. T. Chu, B. E. Little, D. J. Moss, L. Caspani, J. Azaña, and R. Morandotti, "On-chip generation of high-dimensional entangled quantum states and their coherent control," Nature **546**, 622–626 (2017).
16. J. A. Jaramillo-Villegas, P. Imany, O. D. Odele, D. E. Leaird, Z. Y. Ou, M. Qi, and A. M. Weiner, "Persistent energy–time entanglement covering multiple resonances of an on-chip biphoton frequency comb," Optica **4**, 655–658 (2017).
17. J. M. Lukens and P. Lougovski, "Frequency-encoded photonic qubits for scalable quantum information processing," Optica **4**, 8–16 (2017).
18. A. Babazadeh, M. Erhard, F. Wang, M. Malik, R. Nouroozi, M. Krenn, and A. Zeilinger, "High-dimensional single-photon quantum gates: Concepts and experiments," Phys. Rev. Lett. **119**, 180510 (2017).
19. Z. Y. Ou and Y. J. Lu, "Cavity enhanced spontaneous parametric down-conversion for the prolongation of correlation time between conjugate photons," Phys. Rev. Lett. **83**, 2556–2559 (1999).
20. M. Akbari and A. A. Kalachev, "Third-order spontaneous parametric down-conversion in a ring microcavity," Laser Phys. Lett. **13**, 115204 (2016).
21. S. Ramelow, A. Farsi, S. Clemmen, D. Orquiza, K. Luke, M. Lipson, and A. L. Gaeta, "Silicon-nitride platform for narrowband entangled photon generation," arXiv:1508.04358 (2015).
22. C. Simon, M. Afzelius, J. Appel, A. Boyer de la Giroday, S. J. Dewhurst, N. Gisin, C. Y. Hu, F. Jelezko, S. Kröll, J. H. Müller, J. Nunn, E. S. Polzik, J. G. Rarity, H. De Riedmatten, W. Rosenfeld, A. J. Shields, N. Sköld, R. M. Stevenson, R. Thew, I. A. Walmsley, M. C. Weber, H. Weinfurter, J. Wrachtrup, and R. J. Young, "Quantum memories," Eur. Phys. J. D **58**, 1–22 (2010).
23. I. I. Faruque, G. F. Sinclair, D. Bonneau, J. G. Rarity, and M. G. Thompson, "On-chip quantum interference with heralded photons from two independent micro-ring resonator sources in silicon photonics," Opt. Express **26**, 20379–20395 (2018).
24. E. Hemsley, D. Bonneau, J. Pelc, R. Beausoleil, J. L. O'Brien, and M. G. Thompson, "Photon pair generation in hydrogenated amorphous silicon microring resonators," Sci. Rep. **6**, 38908 (2016).
25. J. Leuthold, C. Koos, and W. Freude, "Nonlinear silicon photonics," Nat. Photonics **4**, 535–544 (2010).

26. C. Ma, X. Wang, V. Anant, A. D. Beyer, M. D. Shaw, and S. Mookherjea, "Silicon photonic entangled photon-pair and heralded single photon generation with CAR $>$ 12,000 and $g^{(2)}(0) < 0.006$," Opt. Express **25**, 32995–33006 (2017).
27. W. C. Jiang, X. Lu, J. Zhang, O. Painter, and Q. Lin, "Silicon-chip source of bright photon pairs," Opt. Express **23**, 20884–20904 (2015).
28. J. S. Levy, A. Gondarenko, M. A. Foster, A. C. Turner-Foster, A. L. Gaeta, and M. Lipson, "CMOS-compatible multiple-wavelength oscillator for on-chip optical interconnects," Nat. Photonics **4**, 37–40 (2010).
29. C. Reimer, L. Caspani, M. Clerici, M. Ferrera, M. Kues, M. Peccianti, A. Pasquazi, L. Razzari, B. E. Little, S. T. Chu, D. J. Moss, and R. Morandotti, "Integrated frequency comb source of heralded single photons," Opt. Express **22**, 6535–6546 (2014).
30. D. J. Moss, R. Morandotti, A. L. Gaeta, and M. Lipson, "New CMOS-compatible platforms based on silicon nitride and hydex for nonlinear optics," Nat. Photonics **7**, 597–607 (2013).
31. C. Reimer, M. Kues, P. Roztocki, B. Wetzel, F. Grazioso, B. E. Little, S. T. Chu, T. Johnston, Y. Bromberg, L. Caspani, D. J. Moss, and R. Morandotti, "Generation of multiphoton entangled quantum states by means of integrated frequency combs," Science **351**, 1176–1180 (2016).
32. X. Lu, Q. Li, D. A. Westly, G. Moille, A. Singh, V. Anant, and K. Srinivasan, "Chip-integrated visible–telecom entangled photon pair source for quantum communication," Nat. Phys. **15**, 373–381 (2019).
33. M. H. P. Pfeiffer, A. Kordts, V. Brasch, M. Zervas, M. Geiselmann, J. D. Jost, and T. J. Kippenberg, "Photonic damascene process for integrated high-q microresonator based nonlinear photonics," Optica **3**, 20–25 (2016).
34. M. H. P. Pfeiffer, J. Liu, A. S. Raja, T. Morais, B. Ghadiani, and T. J. Kippenberg, "Ultra-smooth silicon nitride waveguides based on the damascene reflow process: fabrication and loss origins," Optica **5**, 884–892 (2018).
35. M. H. P. Pfeiffer, C. Herkommer, J. Liu, H. Guo, M. Karpov, E. Lucas, M. Zervas, and T. J. Kippenberg, "Octave-spanning dissipative kerr soliton frequency combs in Si_3N_4 microresonators," Optica **4**, 684–691 (2017).
36. J. Liu, A. S. Raja, M. H. P. Pfeiffer, C. Herkommer, H. Guo, M. Zervas, M. Geiselmann, and T. J. Kippenberg, "Double inverse nanotapers for efficient light coupling to integrated photonic devices," Opt. Lett. **43**, 3200–3203 (2018).
37. T. J. Kippenberg, A. L. Gaeta, M. Lipson, and M. L. Gorodetsky, "Dissipative Kerr solitons in optical microresonators," Science **361**, 6402 (2018).
38. V. Brasch, M. Geiselmann, T. Herr, G. Lihachev, M. H. P. Pfeiffer, M. L. Gorodetsky, and T. J. Kippenberg, "Photonic chip–based optical frequency comb using soliton cherenkov radiation," Science **351**, 357–360 (2016).
39. Q. Zhang, C. Langrock, H. Takesue, X. Xie, M. Fejer, and Y. Yamamoto, "Generation of 10-GHz clock sequential time-bin entanglement," Opt. Express **16**, 3293–3298 (2008).
40. M. Savanier, R. Kumar, and S. Mookherjea, "Optimizing photon-pair generation electronically using a p-i-n diode incorporated in a silicon microring resonator," Appl. Phys. Lett. **107**, 131101 (2015).
41. J. Brendel, N. Gisin, W. Tittel, and H. Zbinden, "Pulsed energy-time entangled twin-photon source for quantum communication," Phys. Rev. Lett. **82**, 2594–2597 (1999).
42. M. Caloz, M. Perrenoud, C. Autebert, B. Korzh, M. Weiss, C. Schönenberger, R. J. Warburton, H. Zbinden, and F. Bussières, "High-detection efficiency and low-timing jitter with amorphous superconducting nanowire single-photon detectors," Appl. Phys. Lett. **112**, 061103 (2018).
43. P. Eraerds, N. Walenta, M. Legré, N. Gisin, and H. Zbinden, "Quantum key distribution and 1 Gbps data encryption over a single fibre," New J. Phys. **12**, 063027 (2010).
44. N. Le Thomas, A. Dhakal, A. Raza, F. Peyskens, and R. Baets, "Impact of fundamental thermodynamic fluctuations on light propagating in photonic waveguides made of amorphous materials," Optica **5**, 328–336 (2018).
45. C. Clausen, F. Bussières, A. Tiranov, H. Herrmann, C. Silberhorn, W. Sohler, M. Afzelius, and N. Gisin, "A source of polarization-entangled photon pairs interfacing quantum memories with telecom photons," New J. Phys. **16**, 093058 (2014).
46. S. Tanzilli, H. De Riedmatten, H. Tittel, H. Zbinden, P. Baldi, M. De Micheli, D. B. Ostrowsky, and N. Gisin, "Highly efficient photon-pair source using periodically poled lithium niobate waveguide," Electron. Lett. **37**, 26–28 (2001).
47. N. Bruno, A. Martin, T. Guerreiro, B. Sanguinetti, and R. T. Thew, "Pulsed source of spectrally uncorrelated and indistinguishable photons at telecom wavelengths," Opt. Express **22**, 17246–17253 (2014).
48. P. R. Tapster and J. G. Rarity, "Photon statistics of pulsed parametric light," J. Mod. Opt. **45**, 595–604 (1998).
49. A. Christ, K. Laiho, A. Eckstein, K. N. Cassemiro, and C. Silberhorn, "Probing multimode squeezing with correlation functions," New J. Phys. **13**, 033027 (2011).
50. Z. Vernon, M. Liscidini, and J. E. Sipe, "No free lunch: the trade-off between heralding rate and efficiency in microresonator-based heralded single photon sources," Opt. Lett. **41**, 788–791 (2016).
51. C. C. Tison, J. A. Steidle, M. L. Fanto, Z. Wang, N. A. Mogent, A. Rizzo, S. F. Preble, and P. M. Alsing, "Path to increasing the coincidence efficiency of integrated resonant photon sources," Opt. Express **25**, 33088–33096 (2017).
52. J. Liu, A. S. Raja, M. H. P. Pfeiffer, C. Herkommer, H. Guo, M. Zervas, M. Geiselmann, and T. J. Kippenberg, "Double inverse nanotapers for efficient light coupling to integrated photonic devices," Opt. Lett. **43**, 3200–3203 (2018).
53. Q. Li, M. Davanço, and K. Srinivasan, "Efficient and low-noise single-photon-level frequency conversion interfaces using silicon nanophotonics," Nat. Photonics **10**, 406–414 (2016).